Bias-Free Cardiac Monitoring Capsule

Xuecheng Qu, Sijing Cheng, Ying Liu, Yiran Hu, Yizhu Shan, Ruizeng Luo, Sixian Weng, Hui Li, Hongxia Niu, Min Gu, Yubo Fan, Bojing Shi, Zhuo Liu,* Wei Hua,* Zhou Li,* and Zhong Lin Wang

Cardiovascular disease (CVD) remains the leading cause of death worldwide. Patients often fail to recognize the early signs of CVDs, which display irregularities in cardiac contractility and may ultimately lead to heart failure. Therefore, continuously monitoring the abnormal changes in cardiac contractility may represent a novel approach to long-term CVD surveillance. Here, a zero-power consumption and implantable bias-free cardiac monitoring capsule (BCMC) is introduced based on the triboelectric effect for cardiac contractility monitoring in situ. The output performance of BCMC is improved over 10 times with nanoparticle self-adsorption method. This device can be implanted into the right ventricle of swine using catheter intervention to detect the change of cardiac contractility and the corresponding CVDs. The physiological signals can be wirelessly transmitted to a mobile terminal for analysis through the acquisition and transmission module. This work contributes to a new option for precise monitoring and early diagnosis of CVDs.

1. Introduction

Cardiovascular disease (CVD) remains the leading cause of death worldwide, accounting for ≈32% of all global deaths, with the expectation that this number will rise to >23.6 million deaths annually by 2030.[1,2] Various CVDs often exhibit no obvious symptoms in their early stages, which can be easily overlooked by patients. As these diseases progress to the clinical stage, there is still a significant proportion of patients who do not receive thorough outpatient monitoring and follow-up management, eventually leading to the end stage of cardiovascular disease, known as heart failure (HF).[3,4] Therefore, there is a critical need to identify individuals at high risk for potential cardiovascular diseases at an early stage and give priority to comprehensive and sustainable monitoring during the clinical treatment phase, thereby facilitating treatment implementation, and reducing morbidity and mortality. Currently, although smart watches and wearable vests based on fiber-based technology can monitor physical health indicators (such as ECG: electrocardiogram recording and edema monitoring), their accuracy in diagnosing CVD has not been validated, which provide limited guidance on clinical treatment.[5–8] Small wearable ultrasound patches can provide important cardiac functional parameters and demonstrate excellent portability. However, the processing of data and images is complex, requiring the involvement of skilled technical personnel. Besides, for patients with preheart failure (stage B), symptoms/signs of heart failure were absent while might with the evidence of structural abnormality. For these patients especially in the early stages of impaired cardiac contractility (heart failure), the utility of ultrasound is limited and presents significant constraints.[9,10] Invasive implantable monitoring devices such as CardioMEMS, which monitor pulmonary arterial pressure, can provide effective and accurate pressure parameters to reflect cardiac function indirectly. However, these

X. Qu, Y. Liu, Y. Shan, R. Luo, Z. Liu, Z. Li, Z. L. Wang
Beijing Key Laboratory of Micro-Nano Energy and Sensor
Beijing Institute of Nanoenergy and Nanosystems
Chinese Academy of Sciences
Beijing 101400, China
E-mail: zli@binn.cas.cn; liuzhuo@buaa.edu.cn
X. Qu
State Key Laboratory of Tribology in Advanced Equipment
Department of Mechanical Engineering
Tsinghua University
Beijing 100084, China

S. Cheng, Y. Hu, S. Weng, H. Niu, M. Gu, W. Hua
The Cardiac Arrhythmia Center
State Key Laboratory of Cardiovascular Disease
National Clinical Research Center of Cardiovascular Diseases
Fuwai Hospital
National Center for Cardiovascular Diseases
Chinese Academy of Medical Sciences and Peking Union Medical College
Beijing 100037, China
E-mail: drhuawei@fuwai.com
Y. Hu
Department of Cardiology and Macrovascular Disease
Beijing Tiantan Hospital
Capital Medical University
Beijing 100070, China
Y. Shan, R. Luo, Z. Li
School of Nanoscience and Technology
University of Chinese Academy of Sciences
Beijing 100049, China

**ADVANCED
SCIENCE NEWS**

www.advancedsciencenews.com

**ADVANCED
MATERIALS**

www.advmat.de

types of implantable devices are only suitable for HF patients and have limitations in monitoring the in situ cardiac motion state (Table S1, Supporting Information).[11–13] Various CVDs, including coronary heart disease, cardiomyopathy, arrhythmias, exhibit abnormalities in cardiac contractility. Continual monitoring and detection of the abnormal changes of cardiac contractility could contribute to the early identification of potential CVD patients.[14] Therefore, it is of utmost urgency and importance to develop a novel implantable in situ monitoring device that can accurately and directly reflect the cardiac contractility. Additionally, this device should support continuous and real-time monitoring while being energy-efficient in terms of power consumption.[15,16]

By utilizing the coupling effect of triboelectrification and electrostatic induction, the triboelectric nanogenerator (TENG) is capable of converting mechanical energy directly into electricity.[17] This technology offers several advantages such as high energy conversion rate, material diversity, and simple structure, which has great application prospects in various fields including self-powered sensing,[18–23] new energy,[24–26] and other scenes.[27–30] In recent years, the synergistic development of functional materials, novel mechanisms, and electronic technologies have greatly facilitated advances in personal health monitoring and medical diagnosis.[31–33] These sensors are capable of providing abundant physiological and biomedical information that can be used for sustainable monitoring of individual health.[34–36] On account of the ultrahigh sensitivity and signal-to-noise ratio (SNR), such sensors can even detect weak signals such as sphygmus and respiration.[37,38] The TENG-based self-powered sensor has become a new field of active sensor development. And the usage of materials with good biocompatibility has also greatly promote the application of TENG-based sensor in the field of medical and health, which holds great promise for improving healthcare outcomes and enhancing patient well-being. Despite the significant progress in personal health monitoring, implantable cardiac function monitoring devices based on TENG technology are still restricted by certain limitations, notably their larger size due to device performance. Consequently, a dependence on open-heart surgery persists, leading to heightened risks associated with the implantation procedure.[39] Thus, there is an immediate necessity to create a miniaturized device with enhanced performance capabilities, allowing for more accurate cardiac function monitoring through minimally invasive surgery.

H. Li
Department of Ultrasound
State Key Laboratory of Cardiovascular Disease
National Clinical Research Center of Cardiovascular Diseases
Fuwai Hospital
National Center for Cardiovascular Diseases
Chinese Academy of Medical Sciences and Peking Union Medical College
Beijing 100037, China
Y. Fan, B. Shi, Z. Liu
Key Laboratory of Biomechanics and Mechanobiology
Ministry of Education
Beijing Advanced Innovation Center for Biomedical Engineering
School of Engineering Medicine
Beihang University
Beijing 100191, China
Z. L. Wang
Georgia Institute of Technology
Atlanta, GA 30332-0245, USA

Here, we proposed a simple and effective process to improve the performance indicators of TENG-based sensor, which is particularly suitable for small cavity devices. Compared to untreated device, the process has increased its output voltage by one order of magnitude (5.69 V). Moreover, we specifically designed a bias-free cardiac monitoring capsule (BCMC), with characteristics of miniaturized dimension, high sensitivity, and high SNR (42 dB) for monitoring cardiac contractility. The BCMC measures 6.5 mm in diameter, 20 mm in length, and weighs only 564 mg (Figure S1, Supporting Information), which is small enough to be implanted into the cardiac cavity of animal models through minimally invasive interventions. The device is driven by systole and diastole of the ventricles, causing its internal structure slips and frictions relative to each other to generate electrical signals, which can directly reflect the cardiac contractility, and provide real-time, accurate, and comprehensive monitoring of the cardiac functional status in heart failure patients.

Due to the good sensitivity, high SNR, and fast response of BCMC, the changes of cardiac contractility induced by arrhythmia or positive inotropic drug were successfully monitored through modeling experiment in vivo. Notably, the use of this lightweight catheter-interventional device was safety without complications occurrence in experimental animal. And BCMC is zero-power consumption and can effectively extend the system's lifespan. This device enables continuous and accurate monitoring of cardiac contractility in situ, providing a more stable signal and improving patient compliance. It holds tremendous potential for the early identification of asymptomatic CVD patients with abnormal cardiac contractility, and enables continuous outpatient monitoring of CVD patients undergoing long-term treatment in clinical settings, obviating the need for open surgery. These advancements demonstrate significant promise in the field of implantable medical health monitoring.

2. Results and Discussions

2.1. Cardiovascular Disease Monitoring System (CDMS)

The CDMS consisted of three main components: BCMC sensor, data acquisition/transmission module, and signal wire (**Figure 1a**). The BCMC was delivered into the right ventricle by catheter that could monitor the cardiac contractility, and the signals were transmitted through the subclavian vein via the signal wire to the data acquisition/transmission module located under the subcutaneous tissue. After being processed by hardware, the data were wirelessly transmitted to the mobile terminal. This allowed for real-time display of the cardiac contractility in an intuitive manner. Moreover, doctors can remotely monitor the information for further evaluation and diagnosis (Figure 1b). The shell of the BCMC was fabricated using 3D printing technology with plant-based photosensitive resin, while tungsten rings were incorporated to aid in visualizing the device position in vivo. Additionally, the nickel hooks were utilized to securely fasten the BCMC between muscle bundles in the right ventricle (Figure S2, Supporting Information). The interior of the BCMC featured aluminum films pasted on the wall, with glass pellets filled with polytetrafluoroethylene (PTFE) powder occupying the cavity (Figure 1c). Furthermore, the outermost layer of Parylene C provided good biocompatibility and hydrophobicity properties to
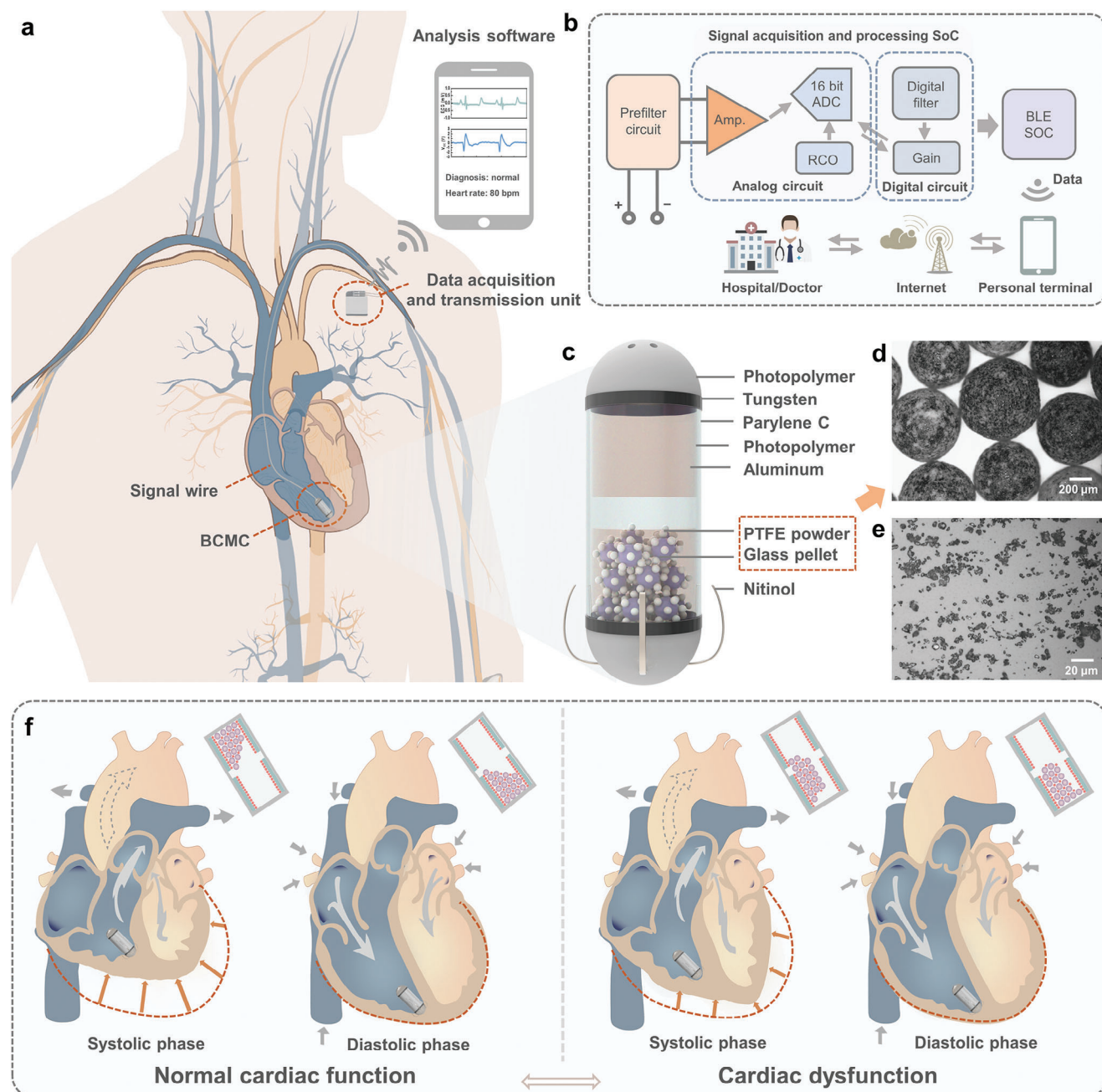
Figure 1. Overview of the cardiovascular disease monitoring system (CDMS). a) Illustration of the bias-free cardiac monitoring capsule (BCMC) in human body. b) Schematic diagram of the signal acquisition and processing. c) Schematic structure diagram of the BCMC. d,e) Microscopy images of glass pellets with polytetrafluoroethylene (PTFE) powder, and PTFE powder, respectively, inner the BCMC (scale bar, 200, and 20 µm, respectively). f) Normal cardiac function/cardiac dysfunction cycle and the corresponding internal motion state of the BCMC.

the device (Figures S3 and S4, Supporting Information). Optical microscopy images corresponding to glass pellets with PTFE powder and PTFE powder were presented in Figure 1d,e, respectively. The cardiac cycle could be divided into systolic and diastolic phases, which drove the BCMC to generate electrical signals that correspond to the cardiac contractility of the heart. Figure 1f depicted the internal states of the device during the periods of normal cardiac function and cardiac dysfunction of heartbeats, respectively.

2.2. Mechanism and Operating Parameters of the BCMC

BCMC is a device that operates on the principle of TENG, coupling by electrostatic induction and triboelectrification in freestanding working mode. The underlying physics can be explained using an extension of Maxwell's equations[40]

$$\varepsilon \nabla \cdot E = \rho - \nabla \cdot P_s \tag{1}$$

$$\nabla \cdot B = 0 \tag{2}$$

$$\nabla \times E = -\frac{\partial B}{\partial t} \tag{3}$$

$$\nabla \times H = J' + \varepsilon\frac{\partial E}{\partial t} + \frac{\partial P_s}{\partial t} \tag{4}$$

$$J_D = \frac{\partial D}{\partial t} = \varepsilon\frac{\partial E}{\partial t} + \frac{\partial P_s}{\partial t} \tag{5}$$

Note that E is the electric field, B stands for the magnetic induction, H means the magnetic field intensity, ρ is the distribution of free charges in space, J means the density of free conduction current density in space as a result of charge flow, t is the time, and D stands for the electric displacement vector. P_s is the polarization density introduced by surface electrostatic charges caused by contact electrification or piezoelectric effect. The addition of the term $\frac{\partial P_s}{\partial t}$ in Maxwell's displacement current provides the fundamental theory behind TENG, which enables the application of Maxwell's equation in the fields of energy and sensing.

Figure 2a,b consisted of a set of comparative schematic diagrams that illustrated the working principle of the sensor. Two aluminum films on the inner wall of the BCMC chamber served as both friction layer and electrode layer. And the glass pellets inside the chamber were used as another friction layer with additional function of power unit. In terms of physical effect, when the glass pellets come into contact with the aluminum film, charges tend to transfer at the interface of the materials due to the contact electrification effect. As a result, aluminum film becomes positively charged while the outer surface of glass pellets become negatively charged. Due to gravity, the glass pellets always tend to stay near the bottom of the chamber, resulting in relative motion with the electrode whenever the BCMC is displaced by an external force such as shaking, presenting a back-and-forth motion between the two electrodes. When the negatively charged glass pellets and the electrodes move relative to each other, the electrostatic balance between the two electrodes will be disrupted, causing a rearrangement of the charge distribution in the electrodes. It will rebalance the electrostatic state and causes charges to transfer in the external circuit, while producing an alternating current.

The output performance of the device is closely related to surface charge density and effective contact area of two friction layers. Here, a rapid processing method has been proposed that involves using nanoscale PTFE powder to electrostatically adsorb it onto the surface of glass pellets. This method could significantly enhance the charge density on the material surface and the effective contact area between the two friction layers. As main power unit, the glass pellets carrying with PTFE ultrafine particles which has strong electronegativity rubbed with the aluminum film, effectively maximize the triboelectric effect between these two friction layers (Figure 2b). Additionally, internal motion process of the device was captured by a high-speed camera, as shown in Figure S5 (Supporting Information).

To ensure optimal output performance of the device, it is important to also consider the size of the glass pellets. As shown in Figure S6 (Supporting Information), when same volume (0.3 cc) of BCMC was used, the open-circuit voltage (V_{OC}), short-circuit current (I_{SC}), and transferred charge (Q_{SC}) were found to strongly negatively correlated with the size of the glass pellets. This is because large-sized glass pellets will hinder their movement inside the cavity due to limited cavity volume, which results in smaller effective contact area with the aluminum electrode. To further investigate the impact of the powder system on device output performance, equal weight powder (1.5 mg) of different materials (PTFE, Polyacrylonitrile (PAN), Polyethylene terephthalate (PET), and Polyadiohexylenediamine (PA66)) were added into the cavity with certain diameter (0.5 mm) and total weight (170 mg) glass pellets.

As shown in Figure S7 (Supporting Information), the output performance of the BCMC was significantly improved when PTFE powder was added, followed by PAN and PET, compared to using only glass pellets in the cavity. The addition of PA66 powder had minimal improvement on the output performance, with V_{OC}, I_{SC}, and Q_{SC} were 1.74 V, 26.01 nA, and 0.51 nC, respectively. Because PTFE has strong electronegativity compared with aluminum and glass, whereas the electropositivity of PA66 is closer to that of aluminum and glass. Further, the relationship between the V_{OC} and filling ratio of glass pellets was also systematically studied, and it was found that the voltage reached its maximum at a filling rate of was 40% glass pellets, after which the output decreased as the pellets increased (Figure 2c). Moreover, the doping ratio of PTFE powder was found to be crucial to the output performance of the BCMC. When the cavity was filled with 40% glass pellets, and mixed with PTFE powder at different mass ratios related to the total mass of glass pellets, the maximum V_{OC} value was achieved at a doping ratio was 2.5%, which was 10 times higher than that without PTFE powder (Figure 2d). The corresponding V_{OC}, I_{SC}, and Q_{SC} were 5.69 V, 77.5 nA, and 1.93 nC, respectively (Figure S8, Supporting Information).

2.3. In Vitro Evaluation of the BCMC

To evaluate the performance of the BCMC device in vivo, various conditions were simulated and tested using a linear motor in vitro. The results showed that the motion angle had a significant impact on output performance of the device, with the effective contact area between friction layers decreasing as the placement angle increased (Figure 2e). At the limit, the V_{OC} of the BCMC was about 137 mV at 90°, which was sufficient for detection. Moreover, the V_{OC}, I_{SC}, and Q_{SC} of the device were positively correlated with the moving distance, indicating that the device's output performance is affected by its movement state (Figure 2f). In addition, the responses of BCMC to external forces under extreme conditions (high frequency and small distance) were also studied, considering the critical significance of output performance and high sensitivity for surveillance purposes. It was determined that the V_{OC} of the BCMC was ≈20 mV under a 10 Hz frequency and 0.25 mm displacement, which is sufficient to accurately detect and monitor an extreme cardiac contractility condition (Figure 2g). Furthermore, even with a movement distance of 3 mm at different frequencies, the BCMC can still acquire high SNR signals (Figure S9, Supporting Information). Additionally, the device also exhibited different output performances with various accelerations (Figure S10, Supporting Information). And the moving speed of the device had a certain influence on its output performance, but the change became slight after the maximum

**ADVANCED
SCIENCE NEWS**

www.advancedsciencenews.com

**ADVANCED
MATERIALS**

www.advmat.de
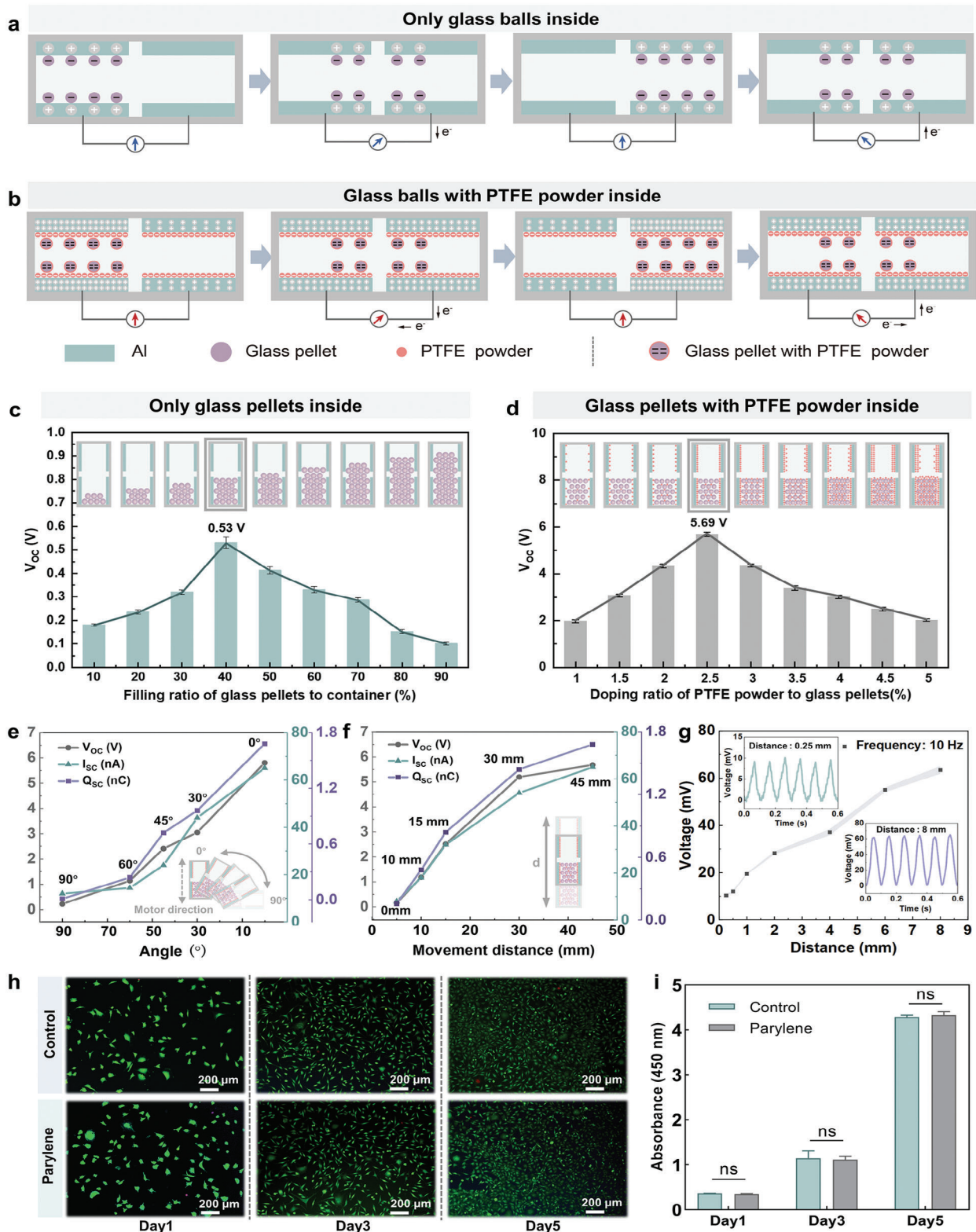
Figure 2. Mechanism and operating parameters of the BCMC. a,b) Schematic diagram of working principle of the BCMC. c,d) V_{OC} of BCMC of nonattached/attached PTFE powder to the glass pellets at different filling/doping ratios (sample size $n = 10$), respectively. e,f) Open-circuit voltage (V_{OC}), short-circuit current (I_{SC}), and transferred charge (Q_{SC}) of the BCMC at different movement angles and distances (frequency, 1.5 Hz). g) V_{OC} of the BCMC at different movement distances (frequency, 10 Hz). h) Fluorescence images of stained L929 cells that were cultured on encapsulation layers of the BCMC (scale bar, 200 μm). i) The normalized viability of L929 cells after being cultured for 5 days ($n = 3$).

speed of 10 m s^{-1} (Figure S11, Supporting Information). Moreover, various frequencies of force were applied to simulate different heart rate states. The result demonstrated a positive correlation between the frequency and output voltage of the BCMC. The time difference between the peaks and peak values of the signals can also serve as an informative parameter, providing an additional dimension of information about the current frequency. These characteristics hold practical significance as they can potentially provide valuable insights into cardiac arrhythmias and cardiac motion state (Figure S12, Supporting Information).

After 10^5 fatigue cycles test, as shown in Figure S13 (Supporting Information), no significant attenuation in the output signal of the device was observed. And after being immersed in normal saline to simulate the conditions in human body for a duration of 36 days, the output performance of the BCMC did not show any noticeable deterioration or significant changes, exhibiting a high level of detection stability (Figure S14, Supporting Information). Additionally, an ultimate stress test was conducted on the BCMC using endocardium of the right ventricle to demonstrate its tensile stability (Figure S15 and Video S1, Supporting Information). Biocompatibility is an essential requirement for implantable medical electronic devices. To evaluate the biocompatibility of the BCMC, L929 cells were used to determine the cytocompatibility of the encapsulation layer. Fluorescence staining was performed at different time intervals (1, 3, and 5 days), and the results showed that the cells attached to the material grew well (Figure 2h,i). Then, the hemolysis and coagulation tests were also carried out on the encapsulation layer. As shown in Figure S16 (Supporting Information), the average hemolysis rate of the material was ≈0.352%, which meets the International Organization for Standardization () standard for implantable medical electronic devices (<5%). Furthermore, Scanning Electron Microscope (SEM) image of platelets adhesion on the encapsulation layer showed that platelets retained a round morphology and did not agglomerate (Figure S17, Supporting Information). In addition, there were no obvious infiltrations of lymphocytes in regional tissues surrounding the BCMC (Figure S18a, Supporting Information), including vital organs – liver, lung, spleen, kidney, and heart (Figure S17b–f, Supporting Information). These results provide evidence that the encapsulation layer of the BCMC possesses excellent cytocompatibility and hemocompatibility, thereby indicating its suitability for secure implantation into the animal body.
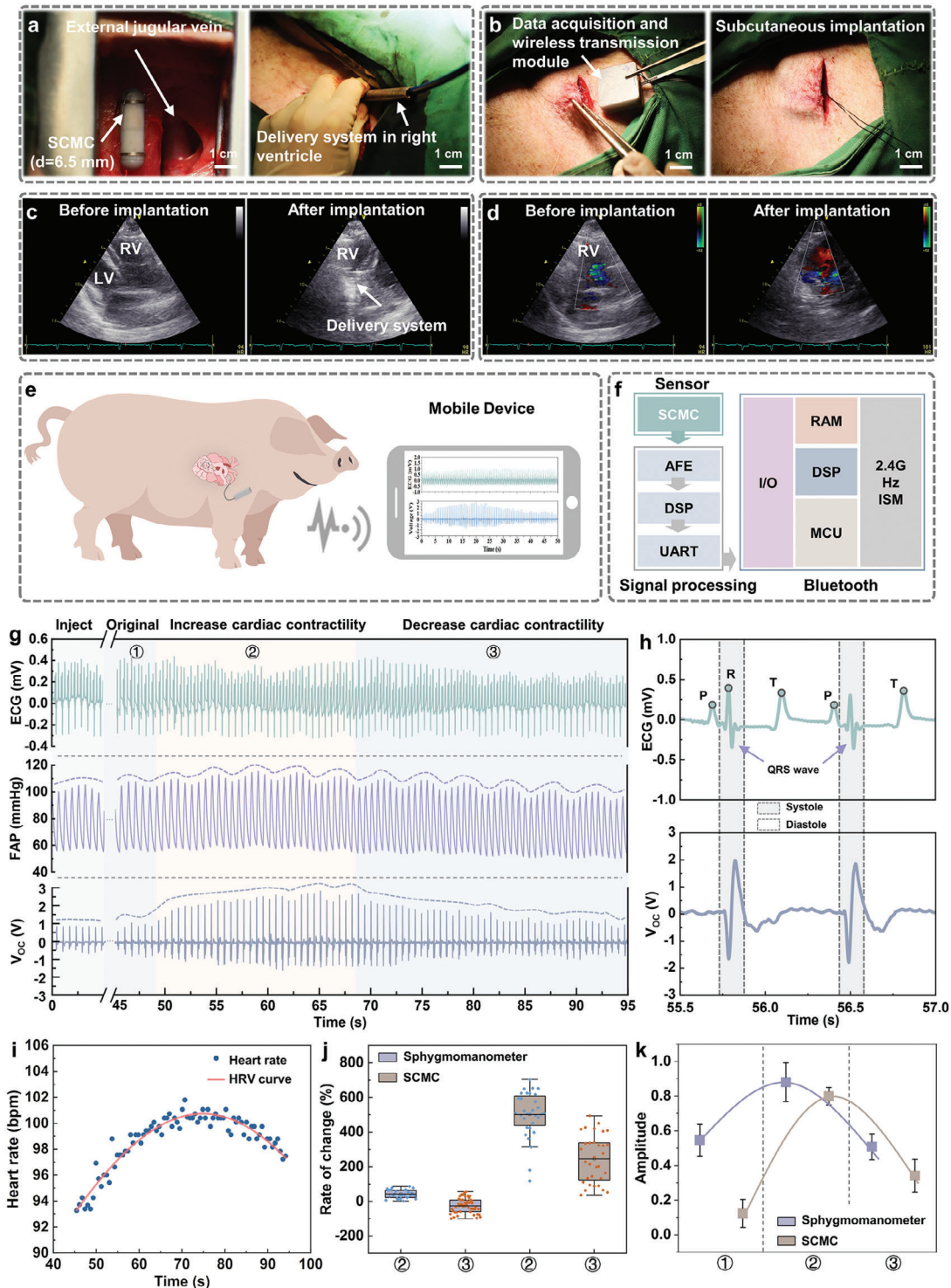
2.4. In Vivo Monitoring of Global Change in Cardiac Contractility Induced by Dopamine Enabled by BCMC

To evaluate the effectiveness of the BCMC for biomedical monitoring in vivo, a study was conducted using a large animal model (swine, female, 70 kg) which involved implanting the BCMC into the right ventricle by a minimally invasive delivery system (**Figures 3a,b** and S19 and Video S2 (Supporting Information)). Successful implantation was achieved with minimal tissue trauma and bleeding through a skin incision of ≈2 cm in length. And the data acquisition/transmission unit were implanted in the subcutaneous tissue. See the Experimental Section for spe-

cific operation process. Fluoroscopic imaging of the device after implantation into the heart was shown in Figure S20 (Supporting Information). Echocardiography performed after the device implantation demonstrated that there were no significant changes in cardiac structures, function, and tricuspid regurgitation (Figure 3c,d and Video S3 (Supporting Information)). The cardiac contraction promoted periodic sliding friction between the glass pellets with PTFE powder and aluminum electrode inside the BCMC, generating the corresponding electrical signals that contained a wealth of physiological parameter information. These signals could be processed and transmitted to the mobile terminal via Bluetooth, allowing for real-time display of the cardiac mechanical activities' status (Figure 3e,f and Figure S21, Table S2, and Video S4 (Supporting Information)).

To investigate the responsiveness of BCMC to changes in cardiac contractility, a moderate dose of dopamine (a kind of positive inotropic agent) was injected into the swine vein to enhance cardiac contractility. The injection process lasted ≈5 s, and after 40 s, the drug started to take effect in contractility. Concurrently, ECG signals, femoral artery pressure (FAP), and V_{OC} of the BCMC were recorded. As shown in Figure 3g, FAP increased slightly with the enhancement of cardiac contractility, as a result of the injection of dopamine (state ① to ②). Then, cardiac contractility gradually returned to the initial state as the efficacy of dopamine disappeared, accompanied by a decline of FAP (state ② to ③, Video S5, Supporting Information). It is noteworthy that changes in cardiac contractility measured by BCMC were almost fully synchronized with dopamine-controlled FAP, demonstrating the feasibility of BCMC as a self-powered sensor for monitoring cardiac contractility.

In addition, electrical signals of the BCMC and ECG were amplified on time axis for comparative analysis (Figure 3h). It could be found that when ventricles contract (QRS complex in ECG), BCMC could simultaneously record the corresponding signal. Furthermore, the intervals between the peaks of the BCMC signal were highly consistent with the intervals between the R peaks of the ECG signal, providing an accurate reflection of the heart rate variability (HRV) for monitoring bradyarrhythmia or tachyarrhythmia. (Figure 3i). Moreover, the normalized signals of FAP and BCMC in Figure 3g were analyzed, respectively. During different periods (states ② and ③), the change rate of the BCMC signal was significantly higher than that of FAP, implying a good sensitivity of the BCMC sensor in response to subtle changes of cardiac contractility (Figure 3j). Similarly, the variation trend of amplitude of the FAP and BCMC signals in different states (states ①, ②, and ③) was demonstrated in Figure 3k, which indicated that the BCMC signal had a better ability to recognize the subtle changes of cardiac contractility caused by CVD in the early stage. It is noteworthy that ECG reflects changes in cardiac electrical activity but cannot directly reflect information about cardiac contractility. Moreover, FAP is an overall indicator affected by many factors. However, BCMC can provide a more intuitive and sensitive way to perceive changes in cardiac mechanical activities' status, and it is less susceptible to the influence of other factors such as respiratory rhythm and autoregulation of blood pressure. Overall, these findings demonstrate the potential utility of the BCMC sensor for monitoring in cardiac mechanical activities' status.

**ADVANCED
SCIENCE NEWS**

www.advancedsciencenews.com

**ADVANCED
MATERIALS**

www.advmat.de

Figure 3. In vivo monitoring of global change in cardiac contractility induced by dopamine enabled by BCMC. a,b) Implantation process of the BCMC in animal experiment. c) 2D transthoracic echocardiography before and after the implantation of the BCMC, showing normal preimplantation cardiac structure, intraoperative device, and delivery system (LV: left ventricle, RV: right ventricle). d) Doppler ultrasound of cardiac before and after the implantation of the BCMC, showing no deterioration of tricuspid regurgitation. e,f) Schematic diagram of signal processing and transmission in vivo experiment. g) Signals of the BCMC in different cardiac contractility statuses in vivo, and the simultaneously recorded signals of electrocardiogram (ECG) and femoral artery pressure (FAP). h) Electrical signals of the BCMC and ECG amplified on time axis. i) Heart rate variability (HRV) reflected by the BCMC signal in (g). j) The relative change rate of the FAP and BCMC signals in increasing cardiac contractility (state ②) and decreasing cardiac contractility (state ③) in (g) (sample size $n = 25$, 32, 25, and 32, respectively). k) The variation trend of amplitude of the FAP and BCMC signals in different states (states ①, ②, and ③) in (g) (sphygmomanometer sample size $n = 6$, 25, 32, and BCMC sample size $n = 6$, 25, 32, respectively).

**ADVANCED
SCIENCE NEWS**

www.advancedsciencenews.com

**ADVANCED
MATERIALS**

www.advmat.de

2.5. In Vivo Monitoring of Regional Change in Cardiac Contractility Caused by Arrhythmia Enabled by BCMC

The arrhythmias are usually caused by excitability of local myocardial cells, or reentry of local myocardial electrical activity, which could decrease the cardiac contractility, thereby affecting hemodynamics.[41] For instance, premature ventricular contraction (PVC) is one of the most common cardiac arrhythmias, caused by abnormal excitation of the local myocardial cells and subsequent ventricular contraction, and manifests as wide and aberrant QRS complex in ECG (**Figures** 4a and S22 (Supporting Information)).[42–44] PVC could impact the regional cardiac contractility. To validate the capability of the BCMC to monitor such common arrhythmia in vivo, a guidewire was implanted via external jugular vein to contact the myocardium for PVC simulation. As shown in Figure 4b, the premature beat was successfully detected by our device, and this could be displayed by a mobile phone in real time. Furthermore, the ECG and FAP signals were recorded synchronously in time with the V_{OC} signal of the BCMC. During the occurrence of PVC, the signals were marked with shading (Figure 4c and Video S6 (Supporting Information)). Notably, while the ECG signal showed typical PVC characteristics, the BCMC signal exhibited downward or of low amplitude peaks. This is due to the fact that PVC decreases the regional cardiac contractility, leading to significant reduction in the signals recorded by BCMC. With advantages of high sensitivity and SNR, the BCMC allowed for detailed recording of these changes in cardiac contractility. Thus, BCMC can effectively detect abnormal local cardiac contractility changes induced by arrhythmia.

Nonsustained ventricular tachyarrhythmia (NSVT) is characterized by more than 3 abnormal PVCs, lasting no more than 30 s, which is one of predictors of sudden cardiac death.[45,46] NSVT manifests as consecutive wide and aberrant QRS complex in ECG, which affects the regional cardiac contractility as well. As shown in shaded part of Figure 4d, the BCMC detected two instances of NSVTs, of which signal clearly recorded the fluctuation and frequency changes of cardiac contractility during NSVT: signal waveform of the BCMC turned to be entirely disorganized in terms of rhythm and amplitude, with a markedly quickened frequency (Figure 4e). These results indicated that the output waveform of the BCMC was closely related to heart rhythm disorder. The BCMC has the potential to record and warn about potential and even fatal arrhythmias, making it a valuable tool for clinical monitoring and diagnosis. This may provide a novel method to facilitate early detection of high-risk individuals for potential cardiovascular diseases and enables comprehensive monitoring and management throughout the entire clinical treatment process, thereby preventing disease progression into heart failure.

3. Conclusion

In this work, a novel bias-free cardiac monitoring capsule was proposed as an ultrasmall and lightweight device for persistently monitoring cardiac contractility. The capsule boasts good sensitivity, high SNR (42 dB), and fast response. The shell of the device was made from biocompatible 3D-printed plant-based photosensitive resin coating with Parylene C. Based on the principle of triboelectric nanogenerator, a self-adsorption method was proposed to improve the output performance (over 10 times) for the device.

In detail, nanoscale PTFE powder was employed to make it electrostatically adsorb onto the surface of glass pellets, which greatly improved the charge density on material surface and increased the effective contact area between two friction layers. Then, the influence of different doping amounts of PTFE powder on output performance of the device was explored. In vitro tests showed that the optimal output voltage reached 5.69 V. Additionally, one of the key features of this device is its self-powered characteristic, allowing for zero-power consumption in the monitoring device part.

Moreover, the long-term reliability and excellent biocompatibility of BCMC also meet the requirements for practical application as an implantable medical monitoring device in vivo. After being implanted into the right ventricle of an adult swine via catheter intervention, the device successfully monitored changes in cardiac contractility as well as PVC, and VT. The signal could be transmitted to the mobile terminal through an integrated acquisition/transmission module implanted under the subcutaneous tissue for monitoring and analyzing of cardiac status in real time. The proposed BCMC enabled accurately and continuously monitoring of cardiac contractility in situ, with more stable signals. This work focuses on the sensor component of the bias-free cardiac monitoring capsule, aiming to provide exceptional performance in monitoring cardiac contractility and achieving zero-power consumption. Our future work will involve strengthening the research on wireless transmission component, and integrating that internally into the capsule. By incorporating near field communication technology, the overall system power consumption will be further reduced while enabling external wireless power supply, which will eliminate the reliance on batteries and further enhance the sustainability of the system. Additionally, the integration of artificial intelligence in the future will contribute to optimizing the current monitoring and treatment management model for patients with CVD. It is expected that this device will definitely show broad prospects in the fields of medical monitoring and diagnosis, which may promote the development of next-generation implantable biomedical device.

4. Experimental Section

Fabrication of the BCMC: The enclosure of the BCMC was 3D printed by photocuring of UV sensitive resins (ANYCUBIC Photon) with good biocompatibility. The overall shape of the enclosure was capsule-like with diameter, length, and wall thickness of 6.5, 20, and 0.5 mm, respectively. Two Al electrodes with microstructure which were sanded by sandpaper (300 mesh) were cut into rectangles and attached to the inner wall of the enclosure, the distance between the two electrodes was 1 mm. The wires were fixed between the aluminum electrodes and the inner wall, and led out of the holes in the top of the enclosure. Glass pellets (diameter: 0.5 mm) were loaded into the cavity as the power unit in motion until they occupied ≈40% of the cavity volume. PTFE powder (particle size: 700 nm) with the mass ratio of 2.5% to the glass pellets was added to the cavity as the friction unit. Narrow strips of tungsten sheet (thickness: 50 µm, width: 1 mm) were rolled into rings and fixed to both ends of the BCMC by adhesive as development marks. Two nickel alloy wires were bent into an arch (diameter: 0.3 mm, length: 10 mm) and crossed through holes in the bottom of the BCMC as the rake to anchor muscle bundles of the right ventricle.

Encapsulation of the BCMC: The ethyl cyanoacrylate (Aibida, Guangzhou, China) was employed as the first package layer to close the seams of the enclosure. Then, the one-component UV light curing

**ADVANCED
SCIENCE NEWS**

www.advancedsciencenews.com

**ADVANCED
MATERIALS**

www.advmat.de
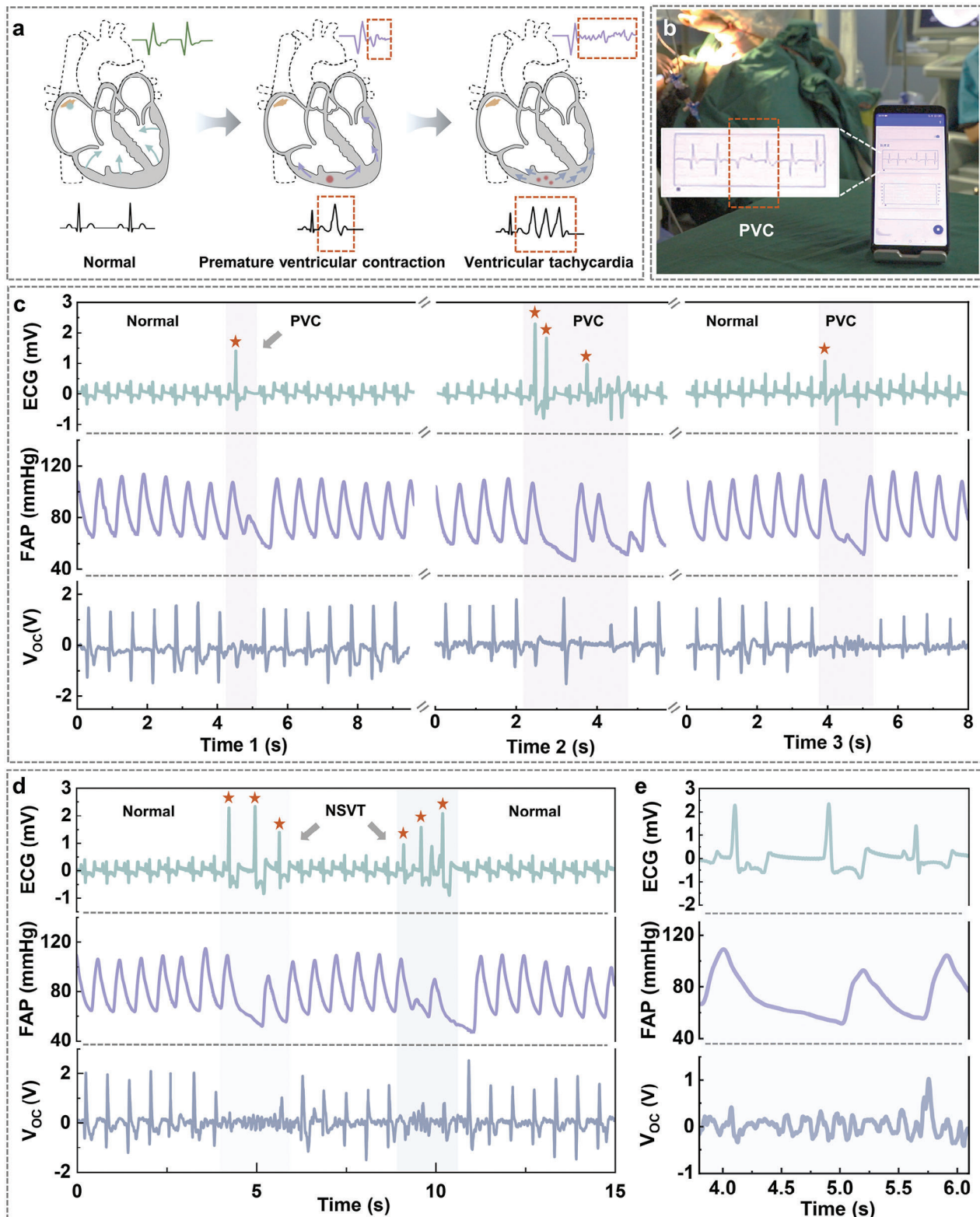
Figure 4. In vivo monitoring of regional change in cardiac contractility caused by arrhythmia enabled by BCMC. a) Characteristics of cardiac contractility under normal sinus rhythm and abnormal arrhythmias, and the corresponding signal characteristics recorded by BCMC. b) Real-time monitoring of premature ventricular contraction (PVC). c) Signals of the BCMC during PVC in vivo, and the simultaneously recorded ECG and FAP signals. d) Signals of the BCMC during nonsustained ventricular tachyarrhythmia (NSVT) in vivo, and the simultaneously recorded ECG and FA4P signals. e) Enlarged view of the shaded part of (d).

adhesive (8500 Metal, Switzerland) was spin-coated on the enclosure as the second package layer and then cured under UV light for 10 s. The holes on the enclosure that led out the wires and fixed the rake needed to be sealed with light-curing glue several times. Finally, the Parylene C particles were steamed at 120 °C and then deposited on the surface of the BCMC, the package thickness of Parylene C was 0.3 μm.

Characterization Methods: Optical photographs of the glass pellets electrostatically absorbed with PTFE powder were exhibited by an optical microscope (Nikon ECLIPSE 3×2 STAGE JAPAN). Optical photographs of the movement of the glass pellets with PTFE powder in the cylinder cavity under simulated device operation were exhibited by high-speed digital video camera (FASTCAM Mini AX200 JAPAN). The output performance (open-circuit voltage, short-circuit current, and transferred charge) of the BCMC was detected by an electrometer (Keithley 6517B) and recorded by oscilloscope (Teledyne LeCroy HD 4096).

Sensitivity Test In Vitro: Vibration table (VT-500, YMC PIEZORONICS. INC.) was employed as a source of mechanical stimuli for sensitivity test (frequency: 5 Hz; operating distance: 0.25–8 mm; frequency: 10 Hz; operating distance: 0.25–8 mm).

Waterproof Test In Vitro: The BCMC was driven periodically by a linear motor to acquire the basic characterization data. The waterproof test in liquid was for stimulating the in vivo environment. The BCMC was fixed at the bottom of the sealed chamber filled with water. The output performance of the BCMC was measured every 9 days in an atmospheric environment (relative humidity 40–50%).

Blood Compatibility: 2 mL fresh blood was obtained from male 6 weeks old SD rats (220 g). 1.5 mL of blood was placed in a centrifuge tube and left for 30 min. The samples were centrifuged at 800 rpm for 10 min. Platelets were removed and placed on the encapsulation material and incubated for 90 min at room temperature. The platelets were fixed with 4% paraformaldehyde (Solarbio, P1110) for 30 min. Serial concentrations of ethanol (50%, 60%, 70%, 80%, 90%, 95%, and 100%) were dehydrated for 30 min and evaporated at room temperature. The surface of the encapsulation material with platelets was visualized by SEM.

Working solution: Positive group: 0.3% Triton X-100 (Solarbio, T8200); negative group: normal saline (0.9% NaCl); material group: 1 mg encapsulation material was immersed in 1 mL of normal saline for 3 days to prepare leaching solution.

The remaining 500 μL of blood was placed in another 15 mL centrifuge tube and washed 4–5 times with 2 mL phosphate-buffered saline (PBS) (1×, Solarbio, P1020) until the supernatant was clear (1000 rpm, 5 min). All red blood cells (RBCs) were resuspended using 5 mL PBS. 0.2 mL resuspended RBCs were mixed with 0.8 mL working solution and incubated for 4 h. The samples were centrifuged at 1000 rpm for 5 min. The supernatant was taken and optical density (OD) value was measured at 541 nm by a microplate reader. %hemolysis = $(OD_{test} - OD_{neg})/(OD_{pos} - OD_{neg})$ × 100%.

Cytocompatibility Test: For the LIVE/DEAD stain, a Calcein-AM/PI Live/Dead double-labeled kit (Solarbio, China) was used. L929 cells were cultured on 96-well plates. The culture dish of the experimental group deposited encapsulation materials. The cells at 1, 3, and 5 days were washed 3 times with PBS solution gently to clear the extracellular esterase activity. After diluting the Calcein-AM solution and propidium iodide (PI) solution into the appropriate concentration with 1× Assay Buffer, the stain solution was added into cells and incubated at 37 °C for 15 min. Then, the cells were observed using an inverted fluorescent microscope (DM6000, Leica, Germany) under 490 ± 10 nm to see the live and dead cells at the same time and 545 nm to see the dead cells only.

The cell counting kit-8 (CCK-8, Solarbio, China) was used for quantify the cell viability on the materials. After removing the culture medium and washing the cells with PBS, a mixture of medium and CCK-8 (ratio: 10:1) solution was added to the cells. After incubation for 2 h, 200 μL culture supernatant was transferred into 96-well plate and the absorbance was measured at 450 nm with a microplate absorbance assay instrument (Biorad iMark, USA).

Histology: The tissues were soaked in a 4% paraformaldehyde overnight at room temperature, then dehydrated with a series of graded ethanol and xylene solutions. Subsequently, routine paraffin embedding was carried out for sectioning at 4 μm. The hematoxylin–eosin and Masson's trichrome staining were employed with standard procedures. The resulting images were observed under a light microscope.

Animal Experiments: The animal experiment was performed by the Nongnong (Beijing) Life & Technology Company and approved by following the Ethical Committee of Animal Experimental Center.

The BCMC Implantation in a Swine Model: The swine (female, 70 kg) was initially anesthetized and intubated with respirators for artificial respiration. Anticoagulant doses of heparin (2000–4000 units) were given intravenously to prevent clot formation. The ECG and FAP were recorded by the data acquisition hardware (MP150 BIOPAC System, INC.). The right-side external jugular vein was exposed with a small incision, then a stiff guide wire (RF*GA35153M: Terumo Corporation, Tokyo, Japan) was inserted to the interior vena cava. Under fluoroscopic guidance, the delivery sheath was advanced into the right ventricle over the guide wire. Then, a manufactured delivery system was carefully advanced across the tricuspid valve, and the BCMC was deployed in the right ventricular apex. After confirming the device with an adequate fixation in endocardium, the delivery system with the sheath was removed from the vein and the incision was sutured.

Induction of Arrhythmia Occurrence in a Swine Model: Arrhythmia was induced by a guide wire via venous system. In detail, the left external jugular vein was punctured and an 8F short sheath (Model HLS-1008 M, Medtronic, Minneapolis, MN, USA) was inserted into it. The guide wire (RF*GA35153M: Terumo Corporation, Tokyo, Japan) was advanced into the sheath to contact the right ventricular myocardium to stimulate PVC. NSVT was induced also by contacting the right ventricular myocardium to stimulate the frequency of PVC over 3 or more consecutive times.

Echocardiographic Examination: Echocardiographic evaluations using the Vivid E95 ultrasound system (GE Vingmend Ultrasound, Horten Norway), including 2D cardiac structure and color Doppler images of tricuspid regurgitation, were measured pre-/postimplantation.

Statistical Analysis: Data were analyzed as mean ± standard deviation. The statistical significance of the differences was determined by a tailed *t*-test. ns was considered no significant differences.

Supporting Information

Supporting Information is available from the Wiley Online Library or from the author.

Acknowledgements

Conflict of Interest

The authors declare no conflict of interest.

Data Availability Statement

The data that support the findings of this study are available from the corresponding author upon reasonable request.

Keywords

**ADVANCED
SCIENCE NEWS**

www.advancedsciencenews.com

**ADVANCED
MATERIALS**

www.advmat.de

[1] G. A. Roth, M. H. Forouzanfar, A. E. Moran, R. Barber, G. Nguyen, V. L. Feigin, M. Naghavi, G. A. Mensah, C. J. L. Murray, *N. Engl. J. Med.* **2015**, *372*, 1333.

[2] G. A. Mensah, G. A. Roth, V. Fuster, *J. Am. Coll. Cardiol.* **2019**, *74*, 2529.

[3] O. Faust, W. Hong, H. W. Loh, S. Xu, R.-S. Tan, S. Chakraborty, P. D. Barua, F. Molinari, U. R. Acharya, *Comput. Biol. Med.* **2022**, *145*, 105407.

[4] S. M. Pogwizd, P. B. Corr, *Circ. Res.* **1987**, *61*, 352.

[5] S. A. Lubitz, A. Z. Faranesh, C. Selvaggi, S. J. Atlas, D. D. McManus, D. E. Singer, S. Pagoto, M. V. McConnell, A. Pantelopoulos, A. S. Foulkes, *Circulation* **2022**, *146*, 1415.

[6] A. Yadollahi, B. Singh, T. D. Bradley, *Ann. Biomed. Eng.* **2015**, *43*, 2131.

[7] P. Pławiak, U. R. Acharya, *Neural Comput. Appl.* **2020**, *32*, 11137.

[8] Y. J. Hong, H. Jeong, K. W. Cho, N. Lu, D.-H. Kim, *Adv. Funct. Mater.* **2019**, *29*, 1808247.

[9] C. Wang, X. Chen, L. Wang, M. Makihata, H.-C. Liu, T. Zhou, X. Zhao, *Science* **2022**, *377*, 517.

[10] H. Hu, H. Huang, M. Li, X. Gao, L. Yin, R. Qi, R. S. Wu, X. Chen, Y. Ma, K. Shi, C. Li, T. M. Maus, B. Huang, C. Lu, M. Lin, S. Zhou, Z. Lou, Y. Gu, Y. Chen, Y. Lei, X. Wang, R. Wang, W. Yue, X. Yang, Y. Bian, J. Mu, G. Park, S. Xiang, S. Cai, P. W. Corey, *Nature* **2023**, *613*, 667.

[11] S. C. Haynes, R. Pallin, K. Tong, S. Henderson, P. S. Romano, *Heart Lung* **2020**, *49*, 251.

[12] L. Perl, D. Meerkin, D. D'amario, B. B. Avraham, T. B. Gal, T. Weitsman, T. Hasin, S. Feickert, G. D'ancona, U. Schaefer, H. Sievert, F. Leyva, Z. I. Whinnett, C. Di Mario, M. Jonas, M. Glikson, M. Habib, O. Caspi, O. Koren, W. T. Abraham, R. Kornowski, F. Crea, *J. Card. Failure* **2022**, *28*, 963.

[13] H. H. Nguyen, I. H. Law, M. W. Rudokas, J. Lampe, T. M. Bowman, G. F. Van Hare, J. N. Avari Silva, *J. Pediatr.* **2017**, *187*, 290.

[14] V. Mani, C. Durmus, W. Khushaim, D. C. Ferreira, S. Timur, F. Arduini, K. N. Salama, *Biosens. Bioelectron.* **2022**, *216*, 114680.

[15] J. Xue, Y. Zou, Y. Deng, Z. Li, *EcoMat* **2022**, *4*, e12209.

[16] Y. Long, J. Li, F. Yang, J. Wang, X. Wang, *Adv. Sci.* **2021**, *8*, 2004023.

[17] Z. L. Wang, *Rep. Prog. Phys.* **2021**, *84*, 096502.

[18] F. Wen, Z. Zhang, T. He, C. Lee, *Nat. Commun.* **2021**, *12*, 5378.

[19] X. Qu, Z. Liu, P. Tan, C. Wang, Y. Liu, H. Feng, D. Luo, Z. Li, Z. L. Wang, *Sci. Adv.* **2022**, *8*, eabq2521.

[20] Y. Yang, X. Guo, M. Zhu, Z. Sun, Z. Zhang, T. He, C. Lee, *Adv. Energy Mater.* **2023**, *13*, 2203040.

[21] Y. Zou, P. Tan, B. Shi, H. Ouyang, D. Jiang, Z. Liu, H. Li, M. Yu, C. Wang, X. Qu, L. Zhao, Y. Fan, Z. L. Wang, Z. Li, *Nat. Commun.* **2019**, *10*, 2695.

[22] H. Guo, X. Pu, J. Chen, Y. Meng, M.-H. Yeh, G. Liu, Q. Tang, B. Chen, D. Liu, S. Qi, C. Wu, C. Hu, J. Wang, Z. L. Wang, *Sci. Rob.* **2018**, *3*, eaat2516.

[23] M. Zhu, Z. Sun, Z. Zhang, Q. Shi, T. He, H. Liu, T. Chen, C. Lee, *Sci. Adv.* **2020**, *6*, eaaz8693.

[24] X. Qu, X. Ma, B. Shi, H. Li, L. Zheng, C. Wang, Z. Liu, Y. Fan, X. Chen, Z. Li, Z. L. Wang, *Adv. Funct. Mater.* **2021**, *31*, 2006612.

[25] D.-M. Lee, N. Rubab, I. Hyun, W. Kang, Y.-J. Kim, M. Kang, B. O. Choi, S.-W. Kim, *Sci. Adv.* **2022**, *8*, eabl8423.

[26] R. Hinchet, H.-J. Yoon, H. Ryu, M.-K. Kim, E.-K. Choi, D.-S. Kim, S.-W. Kim, *Science* **2019**, *365*, 491.

[27] Z.-Y. Huo, D.-M. Lee, J.-M. Jeong, Y.-J. Kim, J. Kim, I.-Y. Suh, P. Xiong, S.-W. Kim, *Adv. Energy Mater.* **2022**, *12*, 2103680.

[28] W. Liu, Z. Wang, G. Wang, G. Liu, J. Chen, X. Pu, Y. Xi, X. Wang, H. Guo, C. Hu, Z. L. Wang, *Nat. Commun.* **2019**, *10*, 1426.

[29] Z. Wen, M.-H. Yeh, H. Guo, J. Wang, Y. Zi, W. Xu, J. Deng, L. Zhu, X. Wang, C. Hu, L. Zhu, X. Sun, Z. L. Wang, *Sci. Adv.* **2016**, *2*, e1600097.

[30] X. Qu, Z. Yang, J. Cheng, Z. Li, L. Ji, *NanoTrends* **2023**, *3*, 100013.

[31] D. Jiang, B. Shi, H. Ouyang, Y. Fan, Z. L. Wang, Z. Li, *ACS Nano* **2020**, *14*, 6436.

[32] G-T. Hwang, H. Park, J.-H. Lee, S. Oh, K.-I. Park, M. Byun, H. Park, G. Ahn, C. K. Jeong, K. No, H. Kwon, S.-G. Lee, B. Joung, K. J. Lee, *Adv. Mater.* **2014**, *26*, 4880.

[33] H. Ryu, H.-m. Park, M.-K. Kim, B. Kim, H. S. Myoung, T. Y. Kim, H.-J. Yoon, S. S. Kwak, J. Kim, T. H. Hwang, E.-K. Choi, S.-W. Kim, *Nat. Commun.* **2021**, *12*, 4374.

[34] Z. Liu, L. Xu, Q. Zheng, Y. Kang, B. Shi, D. Jiang, H. Li, X. Qu, Y. Fan, Z. L. Wang, Z. Li, *ACS Nano* **2020**, *14*, 8074.

[35] Q. Zheng, Y. Zou, Y. Zhang, Z. Liu, B. Shi, X. Wang, Y. Jin, H. Ouyang, Z. Li, Z. L. Wang, *Sci. Adv.* **2016**, *2*, e1501478.

[36] Z. Liu, Y. Ma, H. Ouyang, B. Shi, N. Li, D. Jiang, F. Xie, D. Qu, Y. Zou, Y. Huang, H. Li, C. Zhao, P. Tan, M. Yu, Y. Fan, H. Zhang, Z. L. Wang, Z. Li, *Adv. Funct. Mater.* **2019**, *29*, 1807560.

[37] Z. Liu, Y. Zhou, X. Qu, L. Xu, Y. Zou, Y. Shan, J. Shao, C. Wang, Y. Liu, J. Xue, D. Jiang, Y. Fan, Z. Li, H. Ye, *Research* **2022**, *2022*, 9864734.

[38] X. Qu, J. Xue, Y. Liu, W. Rao, Z. Liu, Z. Li, *Nano Energy* **2022**, *98*, 107324.

[39] H. Ouyang, Z. Liu, N. Li, B. Shi, Y. Zou, F. Xie, Y. Ma, Z. Li, H. Li, Q. Zheng, X. Qu, Y. Fan, Z. L. Wang, H. Zhang, Z. Li, *Nat. Commun.* **2019**, *10*, 1821.

[40] Z. L. Wang, *Mater. Today* **2017**, *20*, 74.

[41] M. M. Casas, R. L. Avitia, F. F. Gonzalez-Navarro, J. A. Cardenas-Haro, M. A. Reyna, *J. Healthcare Eng.* **2018**, *2018*, 2694768.

[42] Y.-M. Cha, G. K. Lee, K. W. Klarich, M. Grogan, *Circ.: Arrhythmia Electrophysiol.* **2012**, *5*, 229.

[43] E. P. Gerstenfeld, T. De Marco, *Circulation* **2019**, *140*, 624.

[44] F. Cools, S. Janssens, A. Vanlommel, A. Teisman, R. Towart, D. J. Gallacher, *J. Pharmacol. Toxicol. Methods* **2011**, *64*, 60.

[45] D. G. Katritsis, W. Zareba, A. J. Camm, *J. Am. Coll. Cardiol.* **2012**, *60*, 1993.

[46] J. L. Sapp, G. A. Wells, R. Parkash, W. G. Stevenson, L. Blier, J.-F. Sarrazin, B. Thibault, L. Rivard, L. Gula, P. Leong-Sit, V. Essebag, P. B. Nery, S. K. Tung, J.-M. Raymond, L. D. Sterns, G. D. Veenhuyzen, J. S. Healey, D. Redfearn, J.-F. Roux, A. S. L. Tang, *N. Engl. J. Med.* **2016**, *375*, 111.